Inorganic Chemistry

Article

pubs.acs.org/IC

High Temperature Structural Study of Gd-Doped Ceria by Synchrotron X-ray Diffraction (673 K ≤ T ≤ 1073 K)

Cristina Artini,*[,†,‡] Marcella Pani,[†] Andrea Lausi,[§] Roberto Masini,[∥] and Giorgio A. Costa[†,⊥]

[†]DCCI, Department of Chemistry and Industrial Chemistry, University of Genova, Via Dodecaneso 31, 16146 Genova, Italy

[‡]CNR-IENI, Via De Marini 6, 16149 Genova, Italy

[§]Elettra-Sincrotrone Trieste S.C.p.A., Strada Statale, 14, km 163.5, 34149 Basovizza Trieste, Italy

[∥]CNR-IMEM, Via Dodecaneso 33, 16146 Genova, Italy

[⊥]CNR-SPIN Genova, Corso Perrone 24, 16152 Genova, Italy

Supporting Information

ABSTRACT: The crystallographic features of Gd-doped ceria were investigated at the operating temperature of solid oxides fuel cells, where these materials are used as solid electrolytes. $(Ce_{1-x}Gd_x)O_{2-x/2}$ samples (x = 0.1, 0.3, 0.5, 0.7) were prepared by coprecipitation of mixed oxalates, treated at 1473 K in air, and analyzed by synchrotron X-ray diffraction in the temperature range 673 K ≤ T ≤ 1073 K at the Elettra synchrotron radiation facility located in Trieste, Italy. In the whole temperature span a boundary was found at x ∼ 0.2 between a CeO_2-based solid solution (for x ≤ 0.2) and a structure where Gd_2O_3 microdomains grow within the CeO_2 matrix, taking advantage of the similarity between Gd^{3+} and Ce^{4+} sizes; the existence of the boundary at x ∼ 0.2 was confirmed also by measurements of ionic conductivity performed by impedance spectroscopy. Similar to what observed at room temperature, the trend of the cell parameter shows the presence of a maximum; with increasing temperature, the composition corresponding to the maximum moves toward lower Gd content. This evidence can be explained by analyzing the behavior of the coefficient of thermal expansion as a function of composition.

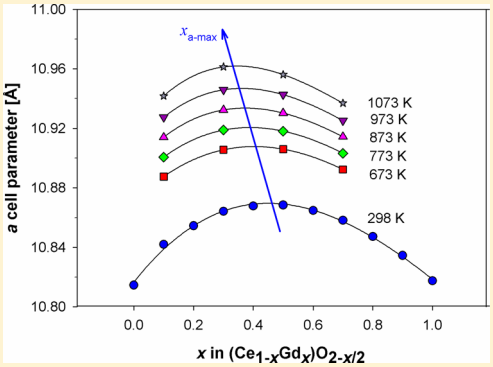

1. INTRODUCTION

The employment of $(Ce_{1-x}Gd_x)O_{2-x/2}$ oxides as electrolytes in solid oxide fuel cells (SOFCs) has been demonstrated to be very promising, especially for $x \leq 0.2$.[1,2] In this compositional region, in fact, their use is particularly advantageous because of their high ion conductivity at intermediate temperatures (800−1000 K), with respect to the well-established yttria stabilized zirconia-based electrolytes, that need higher temperatures (around 1273 K) to work properly.

Fundamental structural issues of this system were debated in the literature for a long time,[3−7] as the size similarity between Ce^{4+} (coordination number, CN, 8) and Gd^{3+} (CN 6) (ionic radius: 0.97 and 0.938 Å, respectively[8]), and the structural resemblance of CeO_2 (space group $Fm\bar{3}m$) and Gd_2O_3 (space group $Ia\bar{3}$), makes it difficult to distinguish whether a solid solution over the whole compositional range or a two-phase region exists. CeO_2 crystallizes in fact in the fluoritic-type cubic structure (hereafter named F), with four CeO_2 formula units per cell,[9] and lattice parameter a = 5.4113(1) Å,[10] where all atoms are sited in special positions, i.e., Ce in (0, 0, 0) and O in ($^1/_4$, $^1/_4$, $^1/_4$); Ce is coordinated to eight O atoms that build edge-sharing cubes. On the other hand, Gd_2O_3 (lattice parameter a = 10.8231(2) Å[11]) crystallizes in a cubic structure (hereafter named C), that can be considered as a fluorite-related arrangement containing one-fourth O atoms less than CeO_2. The removal of the O atoms with respect to CeO_2 causes a split of the crystallographic positions of both the metal and O, and some positional degrees of freedom are introduced. C is a superstructure of F, and due to the fact that the lattice parameter of Gd_2O_3 is exactly double with respect to CeO_2, the peaks common to the two structures appear to be superimposed. This research group recently undertook a structural study of these oxides at room temperature by synchrotron X-ray diffraction[12] and concluded that for 0 ≤ x ≤ 0.3 Gd^{3+} substitutes at Ce^{4+} sites without causing deformations in the host structure, while at higher Gd content, randomly distributed Gd_2O_3 microdomains with C structure grow coherently within the F matrix. A similar conclusion was driven also by Scavini et al.[13] and by Coduri et al.,[14,15] who performed a reciprocal and real space analysis of synchrotron diffraction data collected on Gd-, La-, and Y-doped ceria, respectively; a study on (Yb, Y, La, Nd)-doped ceria was performed too by the same authors.[16] They stated that a biphasic model is needed in order to conveniently interpret the experimental data of these systems; in the case of Ce−Gd oxides, for example, for r ≤ 6 Å (with r = interatomic distance range), i.e., at the nanoscale, the system results in a biphasic structure, namely formed of a fluorite-resembling CeO_2 phase

Received: May 14, 2014
Published: September 5, 2014

   dx.doi.org/10.1021/ic5011242 | Inorg. Chem. 2014, 53, 10140−10149

and a C-Gd_2O_3 resembling phase. However, for $r > \sim 10$ Å the biphasic model does not fit the data, that, on the contrary, match an average model, very similar to the one found by us. It is noteworthy that La_2O_3, stable in a wide temperature range in the hexagonal structure (space group: $P6_3/mmm$), enters the fluoritic structure in the C form to properly fit the CeO_2 crystallographic habit.

The presence of a boundary in the close proximity of $x = 0.2$ is also reported in studies of ionic conductivity.[2,17] The formation of C-Gd_2O_3 microdomains around this composition is considered responsible for the change in the conducting behavior, that shows a nearly constant trend of lattice conductivity from $x = 0$ to $x \sim 0.2$ and a decrease at higher Gd content.[2] Moreover, the maximum of total conductivity shifts toward higher Gd content with increasing temperature. $x \sim 0.2$ represents also a boundary in the conducting behavior when aging effects are taken into account:[17,18] for $x < 0.2$ aged samples show a higher conductivity than unaged ones, while for $x > 0.2$ unaged samples are characterized by higher conductivity.

The structural changes due to the introduction of trivalent rare earths, such as Gd, in the CeO_2 structure, and the formation of defect clusters, have been thoroughly studied also by means of other techniques, such as Raman spectroscopy,[19,20] EXAFS,[21] and atomistic simulations.[22]

The trend of lattice parameters as a function of rare earth amount does not follow Vegard's law, as expected for solid solutions, and does not even show any saturation effect, as would be the case if a two-phase region existed; on the contrary, at room temperature the values show a maximum for $x = 0.45$ and a nearly symmetrical trend as a function of composition.[12] This behavior has been often observed in this system[5,13,23,24] and ascribed to different reasons, such as the ionic repulsion between interstitial anions, the strong interaction between Gd^{3+} and oxygen vacancies, a disorder degree that increases approaching $x = 0.5$, or the possible presence of Ce^{3+}, that is characterized by a ionic size larger than Ce^{4+}. A non-Vegard behavior was observed also in similar systems: Ce−Y,[25] as well as Ce−Dy and Ce−Ho,[26] mixed oxides show a decrease in the lattice parameter of the F structure with incorporation of the trivalent ion, despite the slightly larger ionic radius of the latter with respect to Ce^{4+}; in these cases the unexpected trend is attributed to the incorporation of oxygen vacancies due to the introduction of an aliovalent ion into the parent structure.

Nowadays the crystallographic features of the system at room temperature are widely studied and well-known; nevertheless, structural studies at higher temperature are needed to understand the crystallographic features at the operating temperature of SOFCs. For this reason thermal expansion studies in the present and in similar systems were performed and are documented in the literature.[5,14,25−27] All of them report a decrease in the bulk (i.e., from measurements on massive samples performed by dilatometric analysis), as well as in the lattice thermal expansion, with introducing a rare earth trivalent ion into CeO_2, and this behavior is commonly attributed to the formation of oxygen vacancies that hide the thermal expansion effect.

A detailed study about the effect of temperature on the main parameters determining the structural features of the cited oxides is still lacking; thus, in this work a structural study is presented on a series of four samples analyzed at temperatures ranging between 673 and 1073 K. In order to investigate the existence and the position of the boundary between the CeO_2-based solid solution and the model based on the presence of C-structured Gd_2O_3 microdomains, which is crucial for the conductivity properties of the material, we studied the behavior of several parameters, such as lattice and atomic parameters, the full width at half-maximum (FWHM), and the coefficient of thermal expansion (CTE), as a function of both temperature and Gd content. In order to study a possible correlation between structural and ionic properties, ionic conductivity of samples with x ranging from 0.1 and 0.3 was measured in the 673−1073 K temperature range.

2. EXPERIMENTAL SECTION

2.1. Sample Synthesis. The $(Ce_{1-x}Gd_x)O_{2-x/2}$ powder samples for the crystallographic investigation ($x = 0.1, 0.3, 0.5, 0.7$) were prepared by thermal decomposition of the corresponding coprecipitated mixed oxalates $(Ce_{1-x}Gd_x)_2[C_2O_4]_3{\cdot}nH_2O$, as described in refs 12 and 28. By the same method, a sample with $x = 0.2$ was synthesized for ionic conductivity measurements. The latter were synthesized starting from Ce element (Johnson Matthey ALPHA 99.99% wt) and Gd_2O_3 (Aldrich, 99.99%), by dissolving them in HCl (13% wt) and mixing the two solutions; the coprecipitation was obtained by adding an oxalic acid solution in excess. The oxalate powders were filtered, dried at 350 K in air for 24 h, and subsequently decomposed by thermal treatment at 1473 K in air; the obtained oxides were then slowly cooled in furnace.

2.2. Synchrotron Data Collection. All the samples were analyzed at the powder diffraction beamline (MCX) of the Elettra synchrotron radiation facility located in Trieste, Italy, on a Huber 4-axes X-ray diffractometer equipped with a fast scintillator detector; measurements were performed at temperatures ranging between 673 and 1073 K, making use of a high temperature attachment which allows the instrument to reach temperatures up to 1273 K. Samples were placed in quartz capillary tubes with an inner diameter of 0.5 mm and rotated at a speed of 180 rpm; they were heated in air at 5 °C/min up to the desired temperatures, 673, 773, 873, 973, and 1073 K, and maintained at each temperature for 2 h prior to the acquisition of the patterns. Diffractograms were collected for $5° \leq 2\theta \leq 60°$ with step 0.01°. The incident beam energy has been chosen at 18 keV, with this value being a good compromise between the requirements of the high energy necessary to minimize absorption of the samples, and the spectral characteristics of MCX.

According to the Gd content and to the temperature at which the diffractograms were collected, patterns were named Gd10_673, Gd30_773, and so on. In this Article, when a certain batch is referred to without specification of the test temperature, the name of the sample does not contain any reference to temperature (e.g., Gd10, Gd30, ...). Throughout this work, for sake of comparison, reference is sometimes made to $(Ce_{1-x}Gd_x)O_{2-x/2}$ samples ($x = 0, 0.1, 0.2, 0.3, 0.4, 0.5, 0.6, 0.7, 0.8, 0.9, 1.0$) previously prepared by the same coprecipitation technique and analyzed at room temperature; these samples are the ones described in ref 12 and are hereafter named Ce_298, Gd10_298, and so on.

Data were refined by the Rietveld method by means of the FullProf program.[29]

2.3. Impedance Spectroscopy Measurements. Powders with composition Gd10, Gd20, and Gd30 were pelletized by cold isostatic pressing at 1.5 kbar; the obtained pellets were subsequently sintered at 1923 K for 2 h. They were cut to the proper size for conductivity measurements (~1 mm thickness, ~3 mm diameter), and a Pt paste was applied; they were then dried at 373 K and finally treated at 1273K for 15 min. Ionic conductivities of sintered specimens were measured in the temperature range between 573 and 1073 K in air, making use of a Solartron 1260 impedance analyzer in the frequency range 10^{-1}−10^{6} Hz. Data were fitted by using the Novocontrol WinFit software. SEM photos of polished and thermally etched samples were taken for all the samples in order to evaluate the sintering degree of powders; the density of the sintered pellets was measured by the Archimedes method with toluene.

3. RESULTS

All the diffraction patterns were refined according to the structural model described in ref 12 and reported in Table 1, i.e., a

dx.doi.org/10.1021/ic5011242 | Inorg. Chem. 2014, 53, 10140−10149

Table 1. Structural Model Used for Rietveld Refinements of $Ce_{1-x}Gd_xO_{2-x/2}$ in Comparison with the Two End Member Structures CeO_2 and Gd_2O_3[a]

CeO_2, F structure, *cF*12 $Fm\bar{3}m$ $Z = 4$, $a = 5.4073(1)$ Å			$Ce_{1-x}Gd_xO_{2-x/2}$, starting model for Rietveld refinement, *cI*96 $Ia\bar{3}$ $Z = 32$			Gd_2O_3, C structure, *cI*80 $Ia\bar{3}$ $Z = 16$, $a = 10.8175(1)$ Å		
atom	Wyckoff position	coordinates	atom	Wyckoff position	coordinates	atom	Wyckoff position	coordinates
Ce	4*a*	0, 0, 0	Ce/Gd1	24*d*	*x*, 0, $^1/_4$	Gd1	24*d*	*x*, 0, $^1/_4$
					$x = 0.25$			$x = 0.2815$
			Ce/Gd2	8*a*	0, 0, 0	Gd2	8*a*	0, 0, 0
O	8*c*	$^1/_4$, $^1/_4$, $^1/_4$	O1	48*e*	*x*, *y*, *z*	O	48*e*	*x*, *y*, *z*
					$x = 0.125$			$x = 0.0985$
					$y = 0.375$			$y = 0.3628$
					$z = 0.125$			$z = 0.1287$
			O2	16*c*	*x*, *x*, *x*			
					$x = 0.125$			

[a]From ref 12. Lattice parameters of end members are obtained from the refinements reported in ref 12.

Table 2. Refined Thermal Factors (*B*'s) and Final Agreement Indexes[a]

pattern	B_{RE1} [Å^2]	B_{RE2} [Å^2]	B_O [Å^2]	R_p	R_{wp}	R_B	χ^2
Gd10_673	0.56(1)	0.35(3)	0.95(5)	5.65	7.69	1.46	1.93
Gd10_773	0.51(2)	0.34(4)	1.36(3)	6.27	8.56	1.41	2.34
Gd10_873	0.72(3)	0.66(8)	1.20(5)	5.34	7.08	1.06	1.61
Gd10_973	0.727(3)	0.89(1)	1.51(3)	5.20	6.86	1.11	1.53
Gd10_1073	0.870(3)	0.87(1)	1.54(4)	5.28	6.91	1.50	1.57
Gd30_673	0.97(4)	1.1(1)	1.49(4)	5.70	7.53	1.68	1.57
Gd30_773	1.10(3)	1.28(9)	1.92(4)	5.39	7.32	1.62	1.41
Gd30_873	1.14(1)	1.50(4)	2.09(4)	5.56	7.49	1.33	1.36
Gd30_973	1.29(2)	1.54(6)	2.19(4)	5.23	7.03	1.38	1.36
Gd30_1073	1.89(2)	1.57(5)	2.66(5)	5.43	7.29	1.33	1.38
Gd50_673	0.922(8)	1.87(3)	0.15(4)	5.99	8.18	3.41	2.42
Gd50_773	1.21(1)	1.91(4)	0.04(4)	6.50	9.37	3.80	3.09
Gd50_873	1.16(9)	2.13(4)	0.84(4)	5.50	7.42	2.55	1.93
Gd50_973	1.32(1)	2.21(4)	1.12(4)	5.31	7.21	2.28	1.78
Gd50_1073	1.38(1)	2.33(4)	1.42(4)	5.17	6.99	1.98	1.67
Gd70_673	0.768(7)	1.97(2)	0[b]	5.22	7.10	2.89	1.83
Gd70_773	0.893(7)	2.13(2)	0.08(4)	5.20	7.03	2.63	1.77
Gd70_873	1.007(8)	2.05(2)	0.39(4)	5.04	6.83	2.59	1.62
Gd70_973	1.084(8)	2.33(3)	0.75(4)	5.08	6.86	2.59	1.61
Gd70_1073	1.343(8)	2.42(3)	1.58(3)	5.03	6.77	2.27	1.49

[a]R_p, R_{wp}, and R_B are the profile, weighted profile, and the Bragg factors, respectively. χ^2 is defined as the square of R_{wp}/R_{exp} ratio. [b]Fixed value (see text).

hybrid F−C structure that accounts for the presence of randomly distributed Gd^{3+} ions coherently growing in the fluoritic matrix. The model consists of the C atomic arrangement, where atoms are located in the ideal positions, i.e., as in the F structure. The validity of the model is supported by the fact that the C structure is a superstructure of fluorite with exactly double cell parameter, and no peak splitting can be observed between F and C structures at any composition. Parameters sensitive to the F → C change (RE1 *x* coordinate [RE ≡ Ce/Gd], O1 atomic coordinates, O2 *x* coordinate, and occupation factors) are allowed to vary.

Peak profiles were fitted using the pseudo-Voigt function, with the background making use of a linear interpolation of a set of ∼70 points taken from the collected spectrum; individual thermal parameters *B* were refined for RE1 and RE2, while a global *B* was assigned to both oxygen atoms. For pattern Gd70_673 B_O has been kept fixed to zero, as the refinement gave a slightly negative value. In the last refinement cycles, besides the structural parameters (lattice parameter, Ce/Gd1 *x* coordinate, O1 atomic coordinates, both the *x* coordinate and the site occupation factor of O2, and the thermal *B* parameters), the scale factor, 5 peak parameters, and the background points were refined. The occupancy of O1, initially allowed to vary, was always found near to 1, and was therefore fixed to unity in the last refinement cycles; in all the samples, moreover, the occupational ratio between Ce and Gd was kept fixed to the nominal value. In Table 2, thermal parameters and final agreement indexes are reported, while Table 3 shows refined lattice parameters and atomic positions; in Figure 1 an example of a Rietveld refinement plot (Gd30_873) is shown.

Density of samples was measured and found close to 91% of the theoretical value. Figure 2 shows a SEM photo taken on Gd10 by backscattered electrons: the average size of grains is around 5 μm.

As an example, impedance plots of sample Gd20 measured at 773 and 873 K are reported in Figure 3. It can be noticed that, as expected, total resistance decreases with increasing temperature.

4. DISCUSSION

The main result reported in ref 12 is that at room temperature the introduction of Gd^{3+} into the CeO_2 fluoritic structure starts to be

dx.doi.org/10.1021/ic5011242 | Inorg. Chem. 2014, 53, 10140−10149

Table 3. Refined Values of Lattice Parameters, Fractional Atomic Coordinates of RE1, O1, O2, and of O2 Site Occupation Factors[a]

pattern	cell param a (Å)	$x_{Ce/Gd1}$	x_{O1}	y_{O1}	z_{O1}	x_{O2}	SOF_{O2}
Gd10_298	10.84200(5)	0.2505(1)	0.1247(8)	0.3835(8)	0.125(1)	0.130(1)	0.982(9)
Gd10_673	10.887 60(1)	0.2493(2)	0.120(1)	0.382(1)	0.124(2)	0.126(3)	0.894(6)
Gd10_773	10.900 65(1)	0.2490(2)	0.123(2)	0.377(2)	0.13(1)	0.13(1)	1
Gd10_873	10.914 06(1)	0.2509(2)	0.1241(9)	0.372(1)	0.118(2)	0.120(2)	0.933(6)
Gd10_973	10.927 44(1)	0.2487(1)	0.124(1)	0.380(1)	0.127(2)	0.126(2)	0.930(9)
Gd10_1073	10.941 74(1)	0.2503(1)	0.132(1)	0.379(1)	0.120(2)	0.124(2)	0.972(6)
Gd30_298	10.864 16(4)	0.254 99(7)	0.118(1)	0.368(1)	0.135(1)	0.1248(6)	0.77(1)
Gd30_673	10.905 57(1)	0.254 48(4)	0.1188(5)	0.3681(5)	0.127(1)	0.132(1)	0.765(6)
Gd30_773	10.918 84(1)	0.253 92(4)	0.117(1)	0.370(1)	0.130(1)	0.124(2)	0.717(6)
Gd30_873	10.932 37(2)	0.253 31(4)	0.1205(8)	0.3718(9)	0.129(1)	0.125(2)	0.738(6)
Gd30_973	10.945 90(2)	0.252 41(6)	0.1228(6)	0.3672(6)	0.1316(8)	0.122(1)	0.741(9)
Gd30_1073	10.961 25(2)	0.2501(1)	0.127(1)	0.369(1)	0.121(2)	0.115(2)	0.729(9)
Gd50_298	10.868 42(5)	0.266 65(5)	0.1109(7)	0.3638(6)	0.130(1)	0.1472(4)	0.59(1)
Gd50_673	10.906 02(2)	0.265 49(2)	0.1122(2)	0.3581(2)	0.1314(3)	0.1516(3)	0.62(2)
Gd50_773	10.918 13(2)	0.264 88(3)	0.1102(3)	0.3580(3)	0.1255(3)	0.1556(4)	0.678(6)
Gd50_873	10.930 27(2)	0.264 62(3)	0.1110(2)	0.3602(2)	0.1289(3)	0.1509(4)	0.597(6)
Gd50_973	10.942 66(2)	0.264 25(3)	0.1123(2)	0.3599(2)	0.1289(3)	0.1498(4)	0.609(6)
Gd50_1073	10.956 11(2)	0.263 70(3)	0.1123(2)	0.3597(3)	0.1270(4)	0.1482(4)	0.600(6)
Gd70_298	10.858 13(6)	0.272 62(4)	0.1055(5)	0.3623(5)	0.1295(7)	0.1535(5)	0.38(1)
Gd70_673	10.892 37(2)	0.271 79(2)	0.1076(2)	0.3562(2)	0.1316(2)	0.1560(4)	0.417(6)
Gd70_773	10.903 26(2)	0.271 52(2)	0.1067(2)	0.3557(2)	0.1300(2)	0.1588(4)	0.426(6)
Gd70_873	10.914 33(2)	0.271 61(2)	0.1072(2)	0.3568(2)	0.1315(3)	0.1574(5)	0.426(6)
Gd70_973	10.925 20(3)	0.271 25(2)	0.1074(2)	0.3564(2)	0.1317(3)	0.1574(5)	0.411(6)
Gd70_1073	10.936 90(3)	0.271 12(2)	0.1070(2)	0.3581(2)	0.1307(3)	0.1568(5)	0.393(6)

[a]Data at 298 K are taken from ref 11.

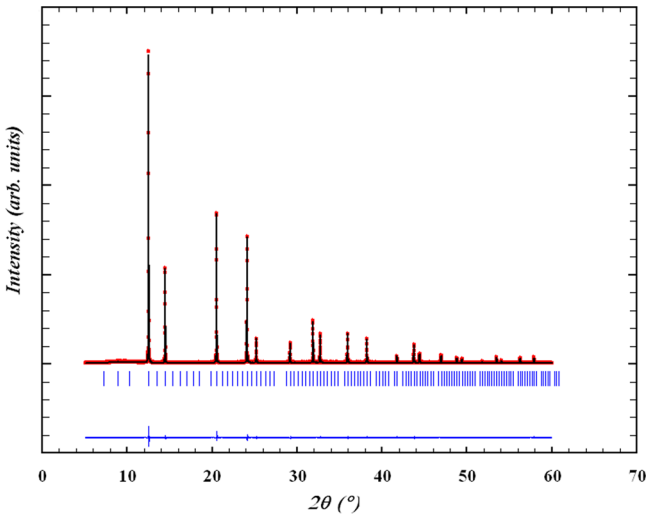

Figure 1. Plot of Rietveld refinement of Gd30_873. The dotted (red) and the continuous (black) lines are the experimental and the calculated diffractogram, respectively; the lower line is the difference curve. The vertical bars indicate the calculated positions of Bragg peaks.

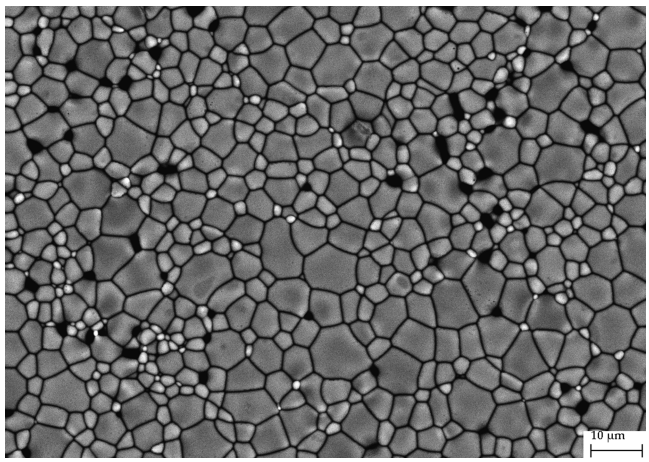

Figure 2. SEM micrograph taken by backscattered electrons of samp le Gd10 after sintering at 1923 K for 2 h.

observable for $x > 0.2$, where the entrance of the trivalent ion with the oxygen vacancies compensates for the valence difference between the two cations; Gd^{3+} uses the fluoritic structure as a matrix, so that the structure can be described by a hybrid model consisting of the C structure with atoms set in the ideal positions, i.e., as in CeO_2. The progressive substitution of Gd^{3+} causes the displacement of Ce/Gd1 and the emptying of the O2 position. For $x \leq 0.2$, on the contrary, Gd^{3+} enters the fluoritic structure of CeO_2 forming a solid solution, and as a consequence the position of Ce/Gd1 and the occupation of O2 do not change significantly. This interpretation is in agreement with the results of our ionic conductivity measurements, that highlight the presence of a boundary at $x = 0.2$ in the trend of total conductivity (σ_{TOT}): at this composition the value of σ_{TOT} is the highest at each temperature considered. Moreover, the Arrhenius plot shows that Gd20 is characterized by a 2-fold behavior: depending on temperature, the conductivity mechanism of Gd20 resembles those of samples at lower and higher Gd content, thus confirming its boundary position. The presence of the boundary close to $x = 0.2$ confirms the results of the analysis performed by Tianshu et al.,[2] who state that both total (σ_{TOT}), as well as lattice (σ_L), conductivities show a dependence on Gd content for each temperature considered: a steep decrease in $\ln(\sigma_{TOT})$ and $\ln(\sigma_L)$ is observed for $x > \sim 0.2$, i.e., starting from compositions where the intergrowth of C-Gd_2O_3 microdomains takes place. The presence of an increasing amount of the microdomains with the

dx.doi.org/10.1021/ic5011242 | Inorg. Chem. 2014, 53, 10140−10149

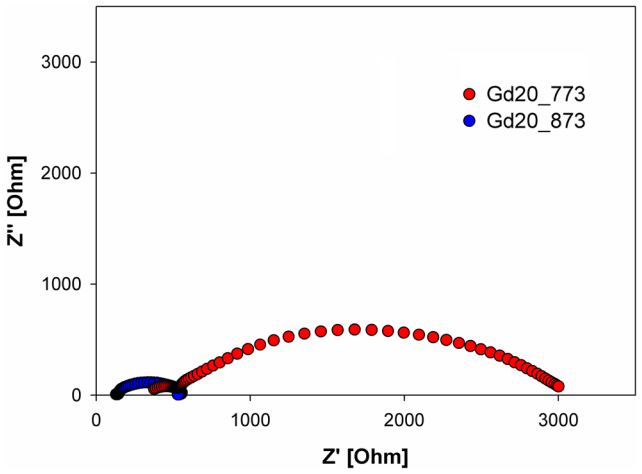

Figure 3. Impedance plots of Gd20 at 773 and 873 K.

increase of the Gd content is in fact believed to exert a blocking effect on the mobility of oxygen ions, responsible for ionic conductivity.

It is noteworthy also that other sesquioxides enter the CeO_2 fluoritic structure in the C form, even though they are more stable in one of the other structural forms typical of rare earth oxides, according to the ionic size of the rare earth. This is for example the case of La_2O_3, which is stable in the A structure (hexagonal, space group $P6_3/mmm$) over a wide temperature span, but enters the CeO_2 matrix in the C form.[14] This evidence suggests that the formation of the hybrid structure is energetically favored with respect to the growth of two phases even when the size difference between Ce^{4+} and the trivalent rare earth ion exceeds the one between Ce^{4+} and Gd^{3+}.

The present study, being performed at high temperature, allows us to extend the knowledge of the crystallographic features of the system at the operating temperatures of SOFCs. In particular, the study was directed toward the detection of the position of the boundary between the two structural models through the analysis of several structural parameters, as well as the analysis of CTE over a wide compositional and temperature range.

4.1. Atomic Structural Parameters and Profile Parameters. Three of the refined parameters gave significant hints, namely the x crystallographic position of RE1, the thermal B factor of oxygen atoms, and the FWHM of the most intense diffraction peak.

The trend of the RE1 x refined position as a function of temperature is shown in Figure 4a, where this parameter, as obtained at 298 K and at higher temperatures, is reported for each composition. The inset of the same figure shows the difference between the values at the minimum (298 K) and the maximum (1073 K) temperature, Δx_T. For $x = 0.1$ no effect of temperature can be recognized, as the refined RE1 x positions oscillate around an average value (0.2498) very close to the one of CeO_2 (0.25), and do not show any regular trend versus temperature. On the contrary, at higher Gd content a trend can be recognized, as from Gd30 to Gd70 the RE1 x position moves toward lower values with increasing temperature, i.e., toward the Ce position in CeO_2, as can be inferred from Table 1. Besides, Δx_T is maximum for Gd30, and decreases with further increasing Gd content, as can be observed in the inset of Figure 4a. This behavior can be understood taking into account that Gd10 is formed of a CeO_2-based solid solution not containing C-

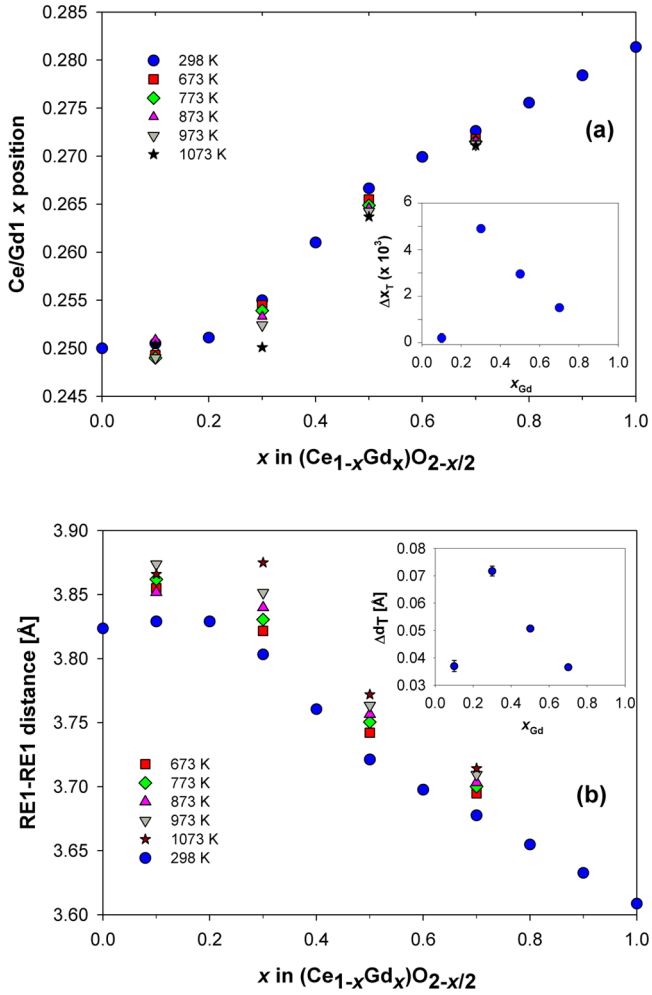

Figure 4. (a) Trend of the Ce/Gd1 x position at 298 K superimposed to the trends of Gd10, Gd30, Gd50, and Gd70 at the different temperatures. Inset shows the difference between values of RE1 x position at 298 K and at 1073 K (Δx_T) as a function of Gd content. (b) Trend of the RE1−RE1 distance as a function of Gd content at 298 K ≤ T ≤ 1073 K, and in the inset the difference between distances at 298 and 1073 K (Δd_T). In both figures error bars are hidden by data markers.

structured microdomains, while from Gd30 to pure Gd_2O_3, the amount of C microdomains growing within the fluoritic matrix increases, becoming dominant at high Gd content. At low Gd content, where the fluoritic structure prevails, the CeO_2 matrix exerts a strong orienting effect on the Gd_2O_3 microdomains, so that with increasing temperature the RE1 x position moves toward the CeO_2 position (see Figure 4a); with increasing Gd content, the amount of Gd_2O_3 microdomains increases too, and the orienting effect of the fluoritic structure becomes weaker, until it disappears at $x_{Gd} = 1$. From the inset it can be noticed that the trend is linear; by extrapolating the regression line at $\Delta x_T = 0$, a value close to 1 (0.87) is found, meaning that the extinction of the orienting effect takes place approaching the Gd_2O_3 composition, thus confirming the interpretation previously given.

In agreement with the previous result, an analogous trend can be observed by analyzing the distances between the rare earth atoms. The transition from the fluoritic-type CeO_2 to the Gd_2O_3 structure causes the shortening of the RE1−RE1 and RE1−RE2 distances (and the relative lengthening of the other conjugate pairs), due to the displacement of RE1 from the ideal position in

dx.doi.org/10.1021/ic5011242 | Inorg. Chem. 2014, 53, 10140−10149

0.25 to ~0.28. In the compositional range of the hybrid structure, the orienting effect of the CeO_2 matrix dominates at low Gd content and increases with increasing temperature, causing a remarkable difference between the distances at 673 and 1073 K. Starting from Gd30, this difference (Δd_T) linearly decreases with increasing Gd content, and the extrapolation of the regression lines at $\Delta d_T = 0$ gives 1.10 and 1.13 for RE1−RE1 and RE1−RE2 distances, respectively. As an example, Figure 4b shows the trend of the RE1−RE1 distance as a function of Gd content, while in the inset Δd_T versus Gd content (x_{Gd}) is reported.

The refined thermal parameters B are reported in Table 2. Two factors contribute to the B parameter, i.e., thermal vibrations and positional disorder, depending on temperature and composition, respectively. As expected, at each composition all B values show an increasing trend with increasing temperature. On the other hand, the influence of composition is visible mainly taking into account the B values of the oxygen atoms. As shown in Figure 5, data associated with Gd50 and Gd70 lie below

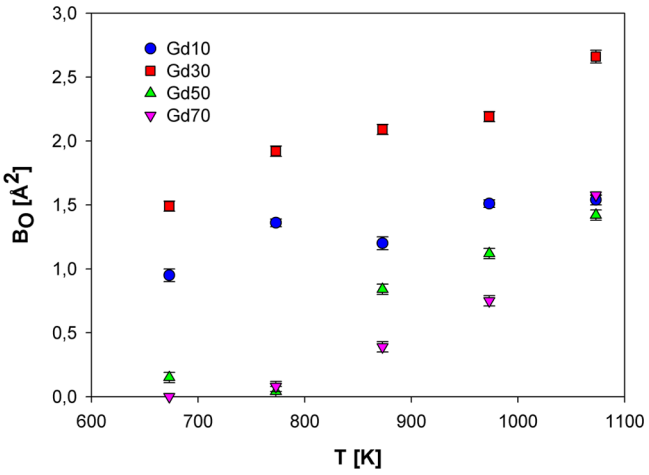

Figure 5. Trend of the oxygen thermal parameters B as a function of temperature for each composition.

Gd10 and Gd30; moreover, they assume values close to zero at the lowest temperatures (673 and 773 K). A possible explanation for this behavior is to consider the blocking effect of the Gd_2O_3 microdomains on the oxygen mobility, acting within the existence range of the hybrid structure; this effect is overcome by thermal vibrations above a certain temperature, so that a steeper increase of B_O appears above 773 K for both Gd50 and Gd70. This phenomenon can be considered as a further confirmation of the presence of the boundary between solid solution and hybrid structure, as well as of the observed decrease in lattice conductivity for $x > \sim 0.2$,[2] that is expected to result in a reduction of positional disorder at low temperature.

The presence of the boundary at $x = 0.3$ is also confirmed by the 2-fold behavior shown by the FWHM of the (222) reflection, corresponding to the most intense peak. The value of FWHM is the result of two factors, namely the crystallite size and the disorder degree: an increase in FWHM can be in fact due to a decrease in the former or to an increase in the latter. For $x = 0.1$ a nearly constant trend appears, while for $x > 0.3$ an increase is found (see Figure 6a). The decreasing trend at $x = 0.3$ can be ascribed to the increasing particle size due to the temperature rise, while for $x > 0.3$ this effect is overcome by the greater disorder degree caused by the intergrowth of C- and F-structured microdomains. This interpretation is qualitatively supported by

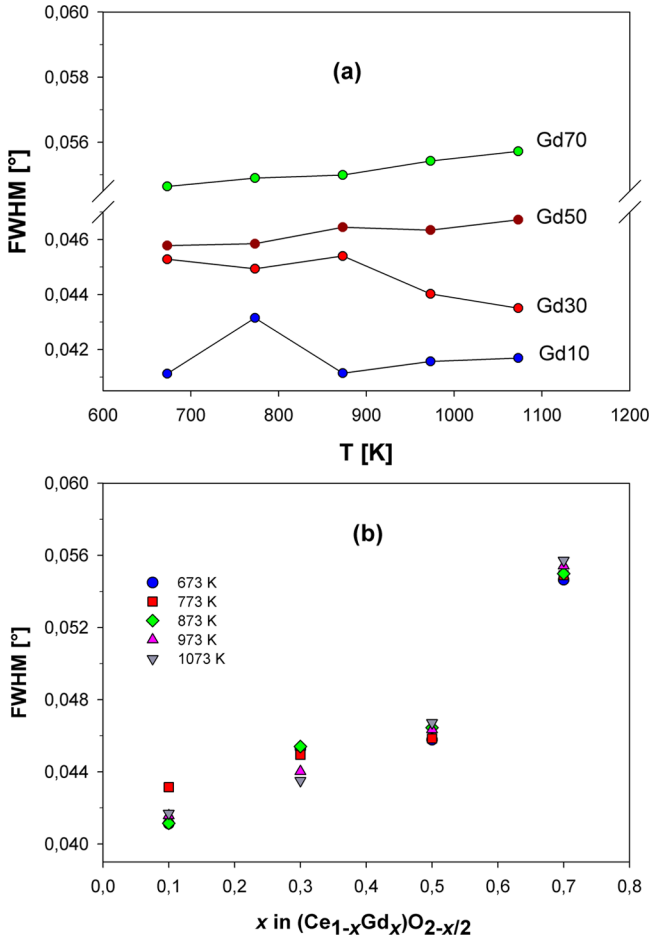

Figure 6. (a) Values of FWHM for the (222) crystallographic planes as a function of temperature (lines are only a guide for the eye) and (b) FWHM values for the (222) crystallographic planes as a function of Gd content at each temperature.

the behavior of FWHM versus Gd amount at each temperature (see Figure 6b): similarly to what already observed at 298 K,[12] a steep increase is visible at high Gd content at each temperature, confirming the presence of a high disorder degree in this region.

4.2. Study of Lattice Parameters and Thermal Expansion Coefficient (CTE). At room temperature the trend of lattice parameters as a function of Gd content shows a maximum for $x \sim 0.5$, and it is nearly symmetrical. The lack of a linear trend throughout the whole compositional range accounts for the absence of a complete solid solution; similarly, the lack of a saturation effect indicates the absence of a two-phase (F + C) region.

A similar trend in the lattice parameters is observable also at higher temperatures, as shown in Figure 7a; it can be noticed that the maximum a value moves toward lower Gd amounts with increasing temperature. The trends of lattice parameters can be fitted by the third degree polynomial functions reported in Table 4, and the maxima, reported in the last column of the table for each fitting curve, show a linear shift from 0.450 at 298 K to 0.346 at 1073 K (Figure 7b).

The behavior of the lattice parameter a as a function of temperature suggests the reason for the observed shift of the maximum. As evident from Figure 8, the lattice parameter linearly increases with increasing temperature at each composition; moreover, at room temperature the value of the lattice parameter rises up to Gd50, and subsequently goes down, in

dx.doi.org/10.1021/ic5011242 | Inorg. Chem. 2014, 53, 10140−10149

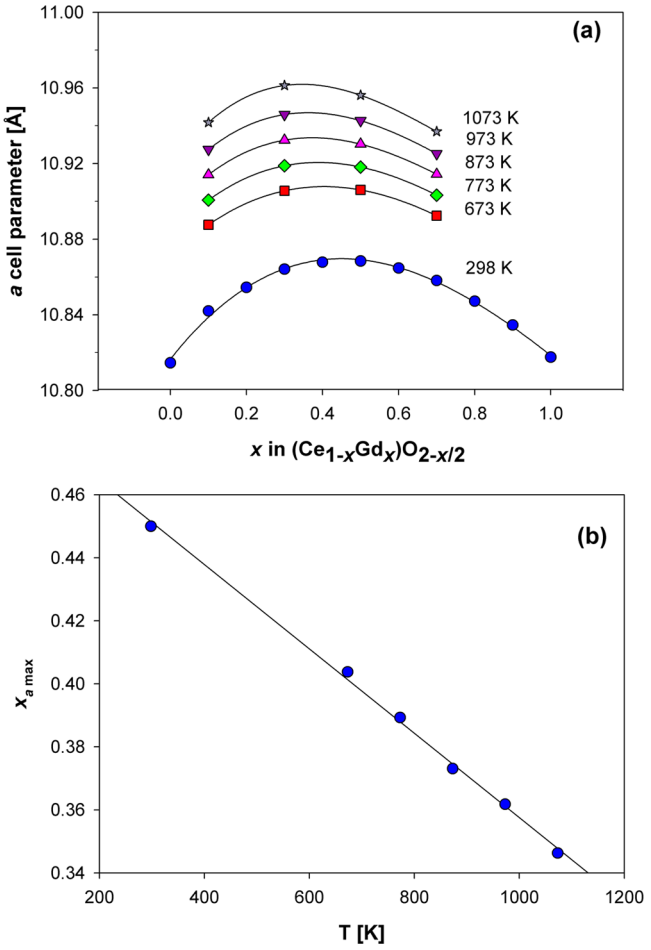

Figure 7. (a) Trend of lattice parameter a as a function of Gd amount for each temperature considered. (b) Trend of x_{amax} (composition at the maximum value of the lattice parameter a) as a function of temperature. In both figures error bars are hidden by data markers.

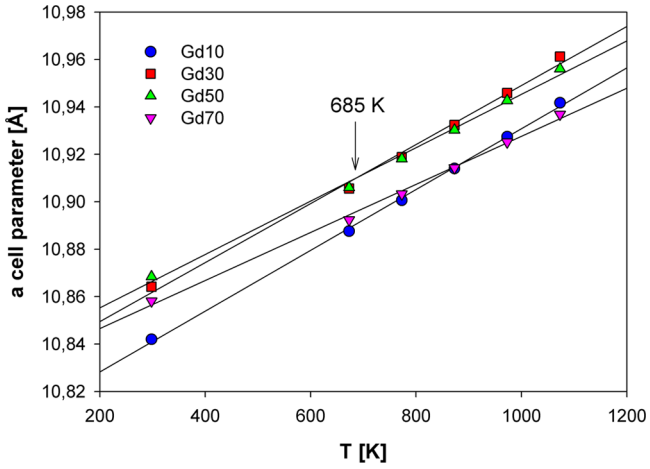

Figure 8. Lattice parameters of all the samples as a function of temperature. Error bars are hidden by data markers.

Table 5. Slope and y-Intercept of Regression Lines $y = mx + b$ of the Lattice Parameters versus Temperature for Each Sample

sample	slope m ($\times 10^4$) (Å K^{-1})	y-intercept b (Å)	R^2
Gd10	1.2822	10.8026	0.999
Gd30	1.2443	10.8246	0.995
Gd50	1.1260	10.8327	0.996
Gd70	1.0139	10.8262	0.997

agreement with the observation of the maximum at $x \sim 0.5$ reported in ref 12. The equations of the regression lines are reported in Table 5: it can be noticed that the slopes decrease with increasing Gd content. In particular, the decrease is linear from Gd30 to Gd70 and steeper than at lower Gd content. These two competing behaviors, namely the decreasing slope and the increasing a value as a function of Gd content, are responsible for the intersection of the Gd30 and Gd50 regression lines, that cross at 685 K; this means that above 685 K Gd30 is characterized by a larger lattice parameter than Gd50.

The shift of the maximum as a function of temperature can be observed also taking into account the behavior of the % lattice thermal expansion (% LTE). It is defined as

$$\%\mathrm{LTE} = 100\frac{(\alpha_T - \alpha_{298K})}{\alpha_{298K}} \quad (1)$$

where a_T and a_{298K} are the values of the cell parameters at the temperature T and at room temperature, respectively. In Figure 9 the % LTE, calculated on the basis of the lattice parameters obtained from the refinements, is plotted for each composition: a linear behavior is observed for each sample, and the corresponding equations of the linear regression lines are reported in Table 6. It can be noticed that the highest value of slope among the compositions studied is related to Gd30, and the difference between the % LTE of Gd30 and Gd50 increases with increasing temperature, thus confirming the shift of the maximum cell parameter value toward the composition with x = 0.3.

Table 4. Polynomial Functions Fitting the Trend of Lattice Parameters at Different Temperatures as a Function of Gd Amount[a]

	fitting function $y = ax^3 + bx^2 + cx + d$					
T (K)	a	b	c	d	R^2	x_{a_max}
298	0.9246×10^{-1}	−0.3450	0.2545	10.8166	0.995	0.450
673	0.7125×10^{-1}	−0.2831	0.1938	10.8710	1	0.404
773	0.9875×10^{-1}	−0.3251	0.2082	10.8830	1	0.389
873	0.1369	−0.3783	0.2251	10.8952	1	0.373
973	0.1558	−0.4115	0.2366	10.9077	1	0.362
1073	0.2204	−0.5065	0.2715	10.9194	1	0.346

[a]In the last column, the value of x corresponding to the maximum a value, x_{a_max}, is reported for each fitting curve. Values at 298 K are taken from ref 12.

dx.doi.org/10.1021/ic5011242 | Inorg. Chem. 2014, 53, 10140−10149

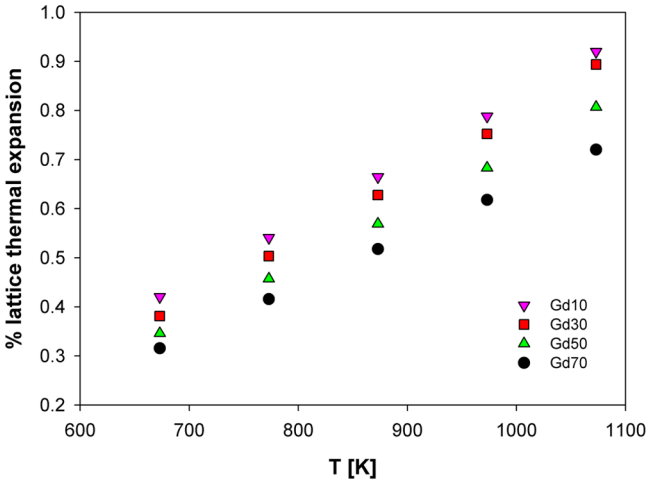

Figure 9. Trend of % lattice thermal expansion vs temperature for samples Gd10, Gd30, Gd50, and Gd70. Error bars are hidden by data markers.

Table 6. Slope and *y*-Intercept of Regression Lines $y = mx + b$ of the % Lattice Thermal Expansion for Each Sample

sample	slope m ($\times 10^3$) (Å K^{-1})	y-intercept b (Å)	R^2
Gd10	1.2457	−0.4207	0.999
Gd30	1.2743	−0.4808	0.999
Gd50	1.1475	−0.4293	0.999
Gd70	1.0119	−0.3660	0.999

A further hint about the position of the structural boundary is provided by the analysis of the Gd30 and Gd10 regression lines of the lattice parameters versus temperature (see Table 5). The intersection between the two lines, in fact, due to the closeness of their slopes (1.2822×10^{-4} for Gd10 and 1.2443×10^{-4} for Gd30), takes place at a very high temperature (~5800 K); as a consequence, the trend of x corresponding to the maximum cell parameter versus T (see Figure 7b) is expected to change for $x < 0.3$. Namely, the decrease is expected to become much softer. The slopes of the cited regression lines are strictly related to the value of the coefficient of thermal expansion (CTE), which, at a certain temperature, is defined as

$$\mathrm{CTE(T)}\frac{1}{\alpha_{298K}} = \frac{(\alpha_T - \alpha_{298K})}{T - 298} \quad (2)$$

where a_T and a_{298K} are the values of the cell parameters at the temperature T and at room temperature, respectively. As reported in the literature, the partial substitution of Ce by a trivalent ion in the CeO_2 matrix causes a decrease in CTE, that takes place when a distortion of the structure occurs due to the introduction of oxygen vacancies. Thus, the x value corresponding to the slope change is the mark of the boundary between the two structural models, namely the solid solution and the hybrid structure based on Gd_2O_3 microdomains, where a significant distortion of the fluoritic matrix takes place. On the basis of the behavior of the lattice parameters versus temperature, an abrupt change in the trend of CTE versus Gd content is expected in correspondence of the boundary.

In order to verify this hypothesis, the behavior of CTE has been studied in more detail, and the values calculated according to eq 2, and referred to the highest temperature (1073 K), are reported in Figure 10 for each sample; furthermore, to make the link between experimental points easier, the literature values of

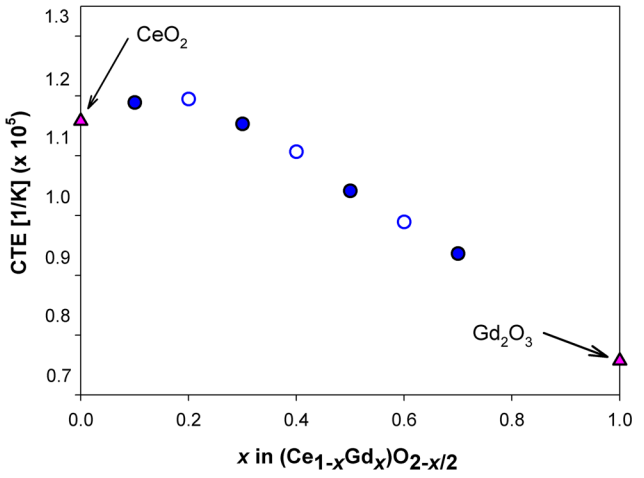

Figure 10. Values of coefficient of thermal expansion (CTE) for samples Gd10, Gd30, Gd50, and Gd70 (●), as obtained from experimental data; ○ symbols represent points at $x = 0.2$, 0.4, and 0.6, calculated from the third-degree functions of Table 5. The triangles at $x = 0$ and $x = 1$ correspond to the literature values of CeO_2[30] and Gd_2O_3,[31] respectively. Error bars are hidden by data markers.

CeO_2[30] and Gd_2O_3,[31] and the additional points at $x = 0.2$, 0.4, and 0.6 (open symbols, obtained from the lattice parameters calculated by using the fitting functions of Table 4), are also plotted in the figure. In the literature a general decrease in CTE due to the substitution of Ce by a trivalent ion has been observed for all the systems examined, as reported for instance by Chavan and Tyagi,[26] who investigated the RE_2O_3−CeO_2 systems (RE ≡ trivalent rare earth ion) at the equimolar composition; this evidence was attributed to the hiding effect on thermal expansion of oxygen vacancies introduced by the substitution. Our study has been conducted on a wider compositional range, and two different trends could be observed, namely a nearly constant value from CeO_2 to Gd20, and a linear decrease from Gd20 to Gd_2O_3. The constant trend of CTE at low Gd amount is related to the existence of the solid solution for $x \leq 0.2$: in this range the CeO_2 fluorite-type structure does not suffer any remarkable distortion. On the other hand, for $x > 0.2$, the displacement of RE1 and the emptying of the O2 position become significant; the composition $x = 0.2$ or its close surroundings thus represent the boundary between the two models. The 2-fold behavior observed suggests that, until the CeO_2-based structure is maintained, the CTE value does not change substantially, but when Gd^{3+} enters the structure modifying it significantly, CTE linearly approaches the value typical of Gd_2O_3. It should be noticed that, only on the basis of the refinement of the structural parameters, a composition in the close surroundings of $x = 0.3$ represents the lower boundary of the hybrid structure or the higher boundary of the solid solution: the transition reveals in fact its effects in a certain composition span, depending on the parameter taken into account. The analysis of the CTE confirms that the boundary is set at $x < 0.3$, namely between $x = 0.2$ and $x = 0.3$, as inferable from Figure 10.

The 2-fold behavior is also in agreement with the results of a study regarding the Nd_2O_3−CeO_2 system[32] where CTE has been investigated for $0 \leq x \leq 0.675$: also in this case a double trend can be recognized around $x = 0.5$, as CTE decreases smoothly for $x < 0.5$ and much more steeply for $x > 0.5$. The boundary between the two different behaviors occurs at the composition where the transition from the F (stable at $x \leq 0.40$) to the C (stable at $x \geq$

dx.doi.org/10.1021/ic5011242 | Inorg. Chem. 2014, 53, 10140−10149

0.50) phase has been found, analogously to the Gd_2O_3−CeO_2 system presented in this work.

4.3. Ionic Conductivity Measurements. Arrhenius plots of total ionic conductivity for samples with x ranging between 0.1 and 0.3 are reported in Figure 11: for x = 0.1 and x = 0.3 all the data can be fitted by the linear functions appearing in Table 7 obtaining R^2 values close to unity; for x = 0.2, on the contrary, in the reported function the point at 673 K is excluded from the set, as the value of $\ln(\sigma_{TOT})$ at the lowest temperature lies well below the trend of data collected at higher temperature. This evidence implies the presence of a critical temperature (T_c) between 673 and 773 K, and it was observed also by Zhang et al.,[17] who noticed the presence of a discontinuity in the σ_L Arrhenius plot of $Ce_{0.8}Gd_{0.2}O_{2-\delta}$ at T = 683 K. They attributed this phenomenon to a 2-fold conductivity behavior in the sample at x = 0.2: at T < 683 K oxygen vacancies combine with Gd^{3+} ions, while above this temperature they do not interact with Gd^{3+} ions, so that their higher mobility degree determines the lower value of activation energy. By closer observation of the fitting functions, it can be noticed that for x = 0.2 the value of the slope (−1.01), referring to data from 773 K to 1073 K, resembles the one reported for x = 0.1 (−1.06), with the absolute value of conductivity being higher for x = 0.2. Between 673 and 773 K, on the contrary, the slope value of the line joining the two points (dash-dotted line in Figure 11) is −1.73, quite similar to what reported for x = 0.3 (−1.47). This means that, between 773 K and 1073 K, the conductivity mechanism is the same for Gd10 and Gd20, and according to the interpretation of Zhang et al.,[17] it is dominated by the presence of mobile vacancies. Due to the higher Gd content, the conductivity value is higher in Gd20 than in Gd10. Below the critical temperature, on the contrary, the conductivity mechanism of Gd20 is similar to the one for Gd30, and it is dominated by the presence of the C-Gd_2O_3 microdomains, that tend to hinder the mobility of oxygen ions, and thus to enhance the activation energy.

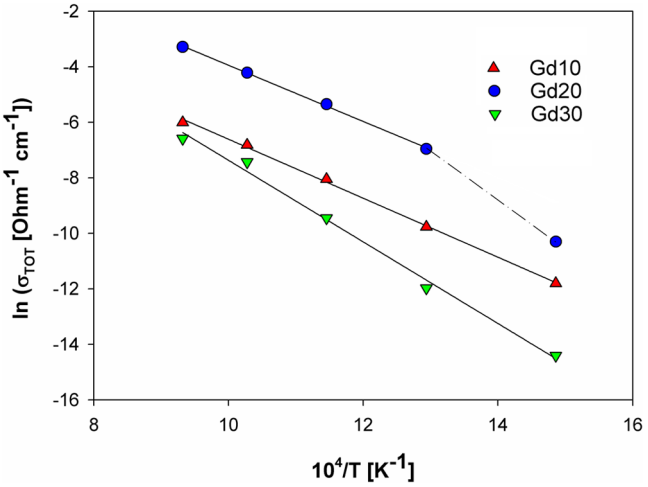

Figure 11. Arrhenius plot of total conductivity for samples Gd10, Gd20, and Gd30. Solid lines fit data points, while the dash-dotted line in sample Gd20 is a guide for the eye joining data at 673 and 773 K.

Table 7. Slope and y-Intercept of Regression Lines $y = mx + b$ of $\ln(\sigma_{TOT})$ as a Function of $10^4/T$ for Each Sample[a]

sample	slope m (×10^4) (K)	y-intercept b	R^2
Gd10	−1.06	4.01	0.998
Gd20	−1.01	6.17	0.999
Gd30	−1.47	7.32	0.994

[a]Regression line of sample Gd20 excludes from the data set the point at T = 673 K.

The behavior of $\ln(\sigma_{TOT})$ as a function of Gd content is reported in Figure 12. It can be observed that the highest value of σ_{TOT} is found for x = 0.2 at each temperature. By calculating the maximum value of the curves joining data in Figure 12, it can be deduced that the composition corresponding to the maximum conductivity value shifts toward higher Gd content with increasing temperature. In the inset to Figure 12 it can be observed that x_{σ_max} increases with temperature, approaching x = 0.2 at 973 K and remaining constant at higher temperature. This fact was already observed by Tianshu et al.,[2] and can be explained taking into account the competing effect of Gd^{3+} doping and temperature increase: with increasing temperature, the amount of Gd^{3+} ions that can be incorporated keeping free the oxygen vacancies increases. Nevertheless, x cannot be indefinitely enhanced, as a value close to 0.2 seems to be the upper limit above which a further increase in Gd content does not produce any increase in conductivity.

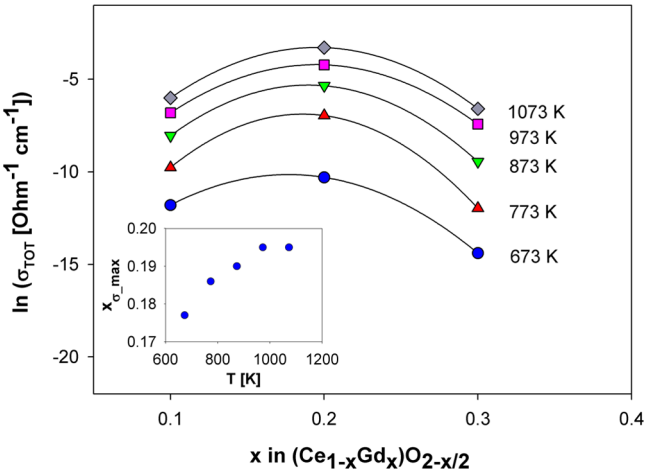

Figure 12. Total conductivity as a function of Gd content from 673 to 1073 K. In the inset the variation of x_{σ_max} vs T is shown.

CONCLUSIONS

A high temperature structural study has been undertaken on samples belonging to the $(Ce_{1-x}Gd_x)O_{2-x/2}$ system in the range 673 K ≤ T ≤ 1073 K, in order to deepen the knowledge of the structural features of these oxides at the operating temperatures of SOFCs. The detailed analysis of several refined parameters, such as the RE1 x position, the B thermal factors and FWHM, as well as the average CTE, suggest the existence of a transition at x ≈ 0.2 from the CeO_2-based solid solution to the CeO_2 matrix with C-Gd_2O_3 embedded particles. The presence of a boundary close to x = 0.2 was also confirmed by impedance spectroscopy measurements: in Gd20 the presence of a critical temperature between 673 and 773 K suggests that the conduction mechanism resembles the one of Gd10 above T_c and the one of Gd30 below T_c. Moreover, the behavior of the lattice parameter as a function of Gd content at the different temperatures considered shows a maximum that shifts toward lower Gd content with increasing temperature; this phenomenon has been explained taking into

dx.doi.org/10.1021/ic5011242 | Inorg. Chem. 2014, 53, 10140−10149

account the linear decrease of CTE from $x > 0.2$ to Gd_2O_3, that in the temperature range studied is responsible for the overcoming of the Gd30 cell parameter with respect to the one of Gd50.

■ ASSOCIATED CONTENT

Supporting Information

Crystallographic data in CIF format and Rietveld plots. This material is available free of charge via the Internet at http://pubs.acs.org.

■ AUTHOR INFORMATION

Corresponding Author

*E-mail: artini@chimica.unige.it. Phone: 0039 010 3536101. Fax: 0039 010 3538733.

Author Contributions

The manuscript was written through contributions of all authors. All authors have given approval to the final version of the manuscript.

Notes

The authors declare no competing financial interest.

■ ACKNOWLEDGMENTS

The Elettra Synchrotron Radiation Facility is kindly acknowledged for the provision of beam time. The authors wish to thank Dr. Jasper Plaisier for assistance in performing measurements at the MCX beamline. Dr. M. T. Buscaglia, Dr. M. Viviani, Dr. F. Perrozzi, and Dr. P. Manfrinetti are kindly acknowledged for their help in performing impedance spectroscopy measurements.

■ REFERENCES

(1) Inaba, H.; Tagawa, H. *Solid State Ionics* **1996**, *83*, 1−16.
(2) Tianshu, Z.; Hing, P.; Huang, H.; Kilner, J. *Solid State Ionics* **2002**, *148*, 567−573.
(3) Bevan, D. J. M.; Summerville, E. In *Handbook on the Physics and Chemistry of Rare Earths*; Gschneidner, K. A., Jr., Eyring L., Eds.; North Holland: Amsterdam, 1979; Vol. 3, pp 401−524.
(4) Brauer, G.; Gradinger, H. *Z. Anorg. Allg. Chem.* **1954**, *276*, 209−226.
(5) Grover, V.; Tyagi, A. K. *Mater. Res. Bull.* **2004**, *39*, 859−866.
(6) Jadhav, L. D.; Chourashiya, M. G.; Jamale, A. P.; Chavan, A. U.; Patil, S. P. *J. Alloys Compd.* **2010**, *506*, 739−744.
(7) Ubaldini, A.; Artini, C.; Costa, G. A.; Carnasciali, M. M.; Masini, R. *J. Therm. Anal. Calorim.* **2006**, *84*, 207−211.
(8) Shannon, R. D. *Acta Crystallogr.* **1976**, *A32*, 751−767.
(9) Eyring, L. In *Handbook on the Physics and Chemistry of Rare Earths*; Gschneidner, K..A., Jr., Eyring L., Eds.; North Holland: Amsterdam, 1979; Vol. 3; pp 337−399.
(10) Varez, A.; Garcia Gonzalez, E.; Sanz, J. *J. Mater. Chem.* **2006**, *16*, 4249−4256.
(11) Heiba, Z.; Okuyucu, H.; Hascicek, Y. S. *J. Appl. Crystallogr.* **2002**, *35*, 577−580.
(12) Artini, C.; Costa, G. A.; Pani, M.; Lausi, A.; Plaisier, J. *J. Solid State Chem.* **2012**, *190*, 24−28.
(13) Scavini, M.; Coduri, M.; Allieta, M.; Brunelli, M.; Ferrero, C. *Chem. Mater.* **2012**, *24*, 1338−1345.
(14) Coduri, M.; Scavini, M.; Brunelli, M.; Masala, P. *Phys. Chem. Chem. Phys.* **2013**, *15*, 8495−8505.
(15) Coduri, M.; Scavini, M.; Allieta, M.; Brunelli, M.; Ferrero, C. *J. Phys: Conf. Ser.* **2012**, *340*, 012056 1−10.
(16) Coduri, M.; Brunelli, M.; Scavini, M.; Allieta, M.; Masala, P.; Capogna, L.; Fischer, H. E.; Ferrero, C. *Z. Kristallogr.* **2012**, *227*, 272−279.
(17) Zhang, T. S.; Ma, J.; Kong, L. B.; Chan, S. H.; Kilner, J. A. *Solid State Ionics* **2004**, *170*, 209−217.
(18) Zhang, T. S.; Ma, J.; Kong, L. B.; Chan, S. H.; Kilner. *Electrochem. Solid State Lett.* **2004**, *7*, J13−J15.
(19) Banerji, A.; Grover, V.; Sathe, V.; Deba, S. K.; Tyagi, A. *Solid State Commun.* **2009**, *149*, 1689−1692.
(20) Grover, V.; Banerji, A.; Sengupta, P.; Tyagi, A. K. *J. Solid State Chem.* **2008**, *181*, 1930−1935.
(21) Deguchi, H.; Yoshida, H.; Inagaki, T.; Horiuchi, M. *Solid State Ionics* **2005**, *176*, 1817−1825.
(22) Minervini, L.; Zacate, M. O.; Grimes, R. W. *Solid State Ionics* **1999**, *116*, 339−349.
(23) Peng, C.; Zhang, Z. *Ceram. Int.* **2007**, *33*, 1133−1136.
(24) Ikuma, Y.; Takao, K.; Kamiya, M.; Shimada, E. *Mater. Sci. Eng.* **2003**, *B99*, 48−51.
(25) Chavan, S. V.; Mathews, M. D.; Tyagi, A. K. *J. Am. Ceram. Soc.* **2004**, *87*, 1977−1980.
(26) Chavan, S. V.; Tyagi, A. K. *Mater. Sci. Eng., A* **2005**, *404*, 57−63.
(27) Mandal, B. P.; Grover, V.; Tyagi, A. K. *Mater. Sci. Eng., A* **2006**, *430*, 120−124.
(28) Costa, G. A.; Artini, C.; Ubaldini, A.; Carnasciali, M. M.; Mele, P.; Masini, R. *J. Therm. Anal. Calorim.* **2008**, *92*, 101−104.
(29) Rodriguez-Carvajal, J. *Physica B* **1993**, *192*, 55−69.
(30) Tyagi, A. K.; Ambekar, B. R.; Mathews, M. D. *J. Alloys Compd.* **2002**, *337*, 277−281.
(31) Momin, A. C.; Mathews, M. D. *Indian J. Chem.* **1977**, *15A*, 1096.
(32) Chavan, S. V.; Mathews, M. D.; Tyagi, A. K. *Mater. Res. Bull.* **2005**, *40*, 1558−1568.